ACS OMEGA

Article

Effect of Metallic Nanoparticles on Improving the Detection Capacity of a Micro-SERS Sensor Created by the Hybrid Waveguide of Metallic Slots and Dielectric Strips

Feng Tang,[†] Salim Boutami,*,[‡] and Pierre-Michel Adam*,[†]

[†]Département de Physique, Mécanique, Matériaux et Nanotechnologies (P2MN), Université de Technologie de Troyes, 12 rue Marie Curie, 10004 Troyes, France

[‡]Université Grenoble Alpes, CEA, LETI, 17 rue des martyrs, 38054 Grenoble, France

Ⓢ Supporting Information

ABSTRACT: The enhancement factor (EF) of surface-enhanced Raman scattering (SERS) mainly depends on the electrical field intensity of surface plasmons in the place of Raman-active molecules. Because of this dependence, the Raman detection sensitivity is much higher with molecules in a small metallic gap than near a single metallic surface because of the intense local electric field resulting from the interaction between metallic objects. In this study, we investigate the SERS detection capacity improved by metallic nanoparticles in a micro-SERS sensor made of a metallic slot and a dielectric strip using the three-dimensional finite-difference time domain method. We calculated the field and charge distributions in the metallic sphere−slot junction to discuss the electromagnetic interaction between the in-sphere localized surface plasmon and the in-slot surface plasmon polariton. After that, the EF dependence of the sensor on the in-slot particle's position, size, shape, and number is demonstrated and discussed to show the strategy of optimizing the SERS detection capacity. It follows the rule that a strong enhancement always appears in a small metallic gap due to the strong field confinement. We show that the averaging SERS enhancement factor around the particle can be increased by 10^5 times, compared to the averaging EF in the slot without metallic nanoparticles that is reported in our previous work, reaching 10^6 (all factors in this study are obtained by the fourth power of the division of the local plasmonic field E_{Loc} to the maximum electric value of the incident light $E_{Inc(max)}$) and at some single points, we have a factor as high as 10^{10}, which is enough to detect a single molecule. With metallic nanoparticles, the micro-SERS sensor can be developed into a highly sensitive tool for the portable and stable Raman detection of molecules or markers in pharmacology, biology, etc.
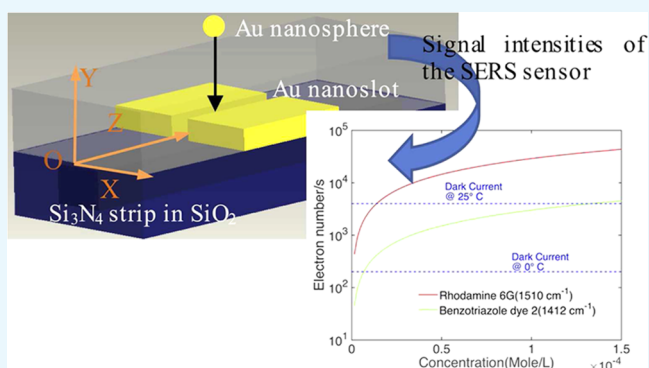
INTRODUCTION

Surface-enhanced Raman scattering (SERS) is widely used as a nondestructive and sensitive spectroscopy technique for detecting molecules' chemical structure with numerous applications like pharmacology, environmental protection, security, etc.[1−5] Compared to the classic Raman scattering, the modified Raman scattering is mainly (excluding the chemical enhancement) enhanced by the intense electric field of surface plasmon polaritons (SPP), which are a collective oscillation of electrons at the interface between materials of opposite permittivities.[6] The polaritons are often categorized into two classes: surface plasmon polaritons (SPP) and localized surface plasmons (LSP). SPP are propagating plasmons at the plane interface between metals and dielectrics. LSP are nonpropagating plasmons on metallic nanoparticles, the sizes of which are smaller than the incident wavelength. They are both widely employed in sensing applications, such as Casein detection in milk[7] and biotinylated bovine serum albumin analysis.[8] LSP are commonly exploited in highly

sensitive Raman detections. In particular, colloidal solutions of aggregated metallic nanoparticles always have very strong enhancement effects due to the intense and strongly confined electric field in the nanogaps between particles (noted as *hotspot effect*). With metallic nanogaps as hotspots, the enhancement factor (EF, which describes the magnification times of SERS signal intensity compared to the non-SERS case) can be higher than 10^9, even enough to detect a single molecule.[9] Meanwhile, in recent years, the advent of integration technologies has facilitated the miniaturization tendency of instrumentation in the optical measurements. Many efforts have been made aiming at miniaturization of Raman detection tools into microdevices by replacing discrete optic elements with integrated photonic circuits.[10−13] Considering the need for chemical and biological detections, on-a-chip SERS detection
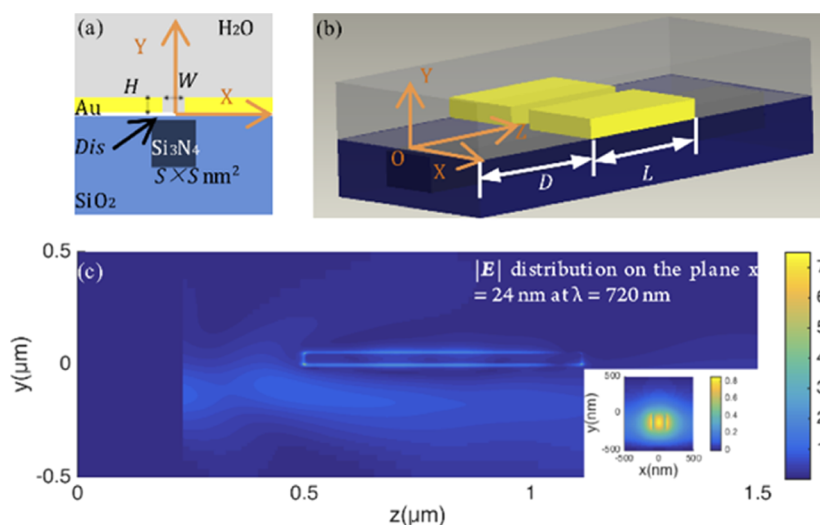
Figure 1. Structure of the SERS sensor: (a) cross section of the hybrid waveguide, where a square Si_3N_4 strip with side S is located at a distance Dis under a gold slot with height H and width W deposited on the silica substrate; (b) 3D view, where one L-length gold slot is laid above the embedded Si_3N_4 strip; (c) $|E|$ field distribution on an x-normal plane with x = 24 nm (across a slot wall) when the fundamental TE mode (as shown in the inset) of the Si_3N_4 strip is injected at z = 0.25 μm as the incidence.

systems with a high enhancement factor are one of the most desirable tools in the near future.

In our previous work, we demonstrated that a micro-SERS sensor based on a hybrid waveguide made of a gold slot and a silicon nitride (Si_3N_4) strip can conduct SERS detections.[14] The SERS enhancement mainly comes from the plasmonic field of the in-slot SPP excited by the evanescent field of the photonic mode of the Si_3N_4 strip.[15] As we have reported earlier in our sensor, a portion 20−60% of the incident power can be transformed into the slot's plasmonic mode from the in-strip photonic mode. More details about the sensor can be found in ref 14. The sensor, with the integration with a microlaser and a microspectrometer, can be developed into a fully integrated on-a-chip Raman detection system. However, this sensor only possesses a mild enhancement, such as 10^2−10^3 around the slot corners, not enough for low-concentration or single-molecule detections. A method is proposed in this study to improve further the SERS detection capacity of the sensor.

Interestingly, it has been already shown that the LSP in metallic nanoparticles can be excited by the SPP propagating on a metallic surface or in a metallic wire.[16−20] If the gap in the particle surface/wire junction is small enough, then the local plasmonic field inside will be so intense that Raman scatterings can be enhanced dramatically. For example, a Ag nanoparticle wire junction with a 1 nm wide gap can be SERS hotspots with a high sensitivity down to a few molecules detection.[20] Its enhancement factor can be as high as the levels achieved in colloidal solutions of aggregated metallic nanoparticles. Besides that, the coupling between SPP and LSP also provides an approach to excite LSP in nanoparticles with a confined field incidence from a remote source. Therefore, the SPP−LSP coupling is a possible strategy to our sensor for further enhancing Raman scatterings signals.

Being encouraged by the initial results[14] and by the SPP−LSP coupling, we numerically investigated in this study the improvement of the SERS detection capability by placing metallic nanoparticles into the metallic slot of the sensor, using the three-dimensional finite-difference time domain (3D-FDTD) method. With SPP as the excitation source, the plasmon modes (localized SPP−LSP modes) of a gold sphere−

slot junction are discussed systematically with the absorption spectra and the local field/charge distributions. Compared to the excitation of the sphere in free space, the electron oscillations of the in-slot sphere, which is excited by the SPP in a finite metallic slot, have an obvious difference. To show the strategy of optimizing the sensor's detection capacity, the dependence of the enhancement factors around the in-slot particle on the particle's position, size, shape, and number is investigated. Generally, a particle−slot junction with suitably sized gaps can provide an averaging EF around 10^6 if all sites in the junction are covered by Raman-active analytes.

The geometry of the SERS sensor is shown in Figure 1. The hybrid waveguide of the sensor has a cross section shown in Figure 1a, where a gold slot with H = 50 nm and W = 48 nm is laid on the SiO_2 substrate, in which a square Si_3N_4 strip with side S = 200 nm is embedded below vertically at a depth Dis = 10 nm. Gold and silicon nitride (Si_3N_4) are specially chosen as the materials to design the SERS sensor. Gold is one of the most promising metals for plasmonics in the red and near-infrared range, together with a high chemical stability. Silicon nitride (Si_3N_4) is almost transparent in the visible and near-IR spectra with a high dielectric constant ε = 4, which ensures a good confinement of light fields. Water is taken as the superstrate material, which is the environment of the excitation and radiation of induced Raman dipoles in molecules if analytes are dissolved in water. The frame of the sensor is presented in Figure 1b. We set D = 0.5 μm and the length of the slot L = 0.61 μm, which is one period of energy exchange between the slot and the strip in the hybrid waveguide at λ = 720 nm. According to the field properties of surface plasmons (being perpendicular to metallic surfaces), only the TE mode ($E_x > E_y$, E_z) of the strip can interact with the plasmonic mode in the metallic slot. The fundamental TE mode of the isolated strip is obtained by the mode eigensolver of the software and it is used as the incident light. To conduct a SERS signal detection, the incident light is injected into the Si_3N_4 strip. Then, it couples into the gold slot and excites the in-slot propagating SPP, which can induce Raman dipoles in Raman-active molecules in the slot. The radiation of induced Raman dipoles in the slot can excite plasmonic modes guided in the slot and then the
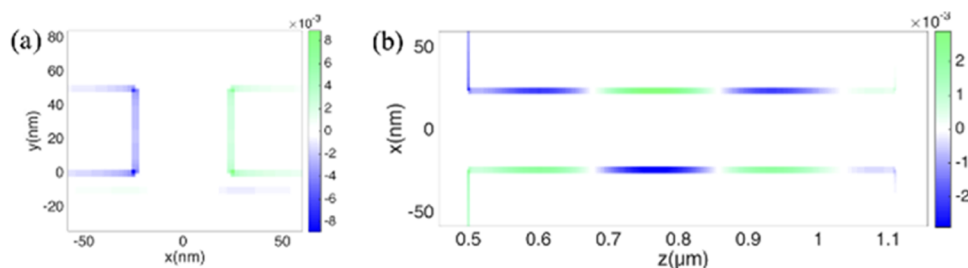
Figure 2. Charge distributions of the SERS sensor (a) on a z-normal plane with $z = 0.805$ μm and (b) on a y-normal plane with $y = 22$ nm. The wavelength is 720 nm.
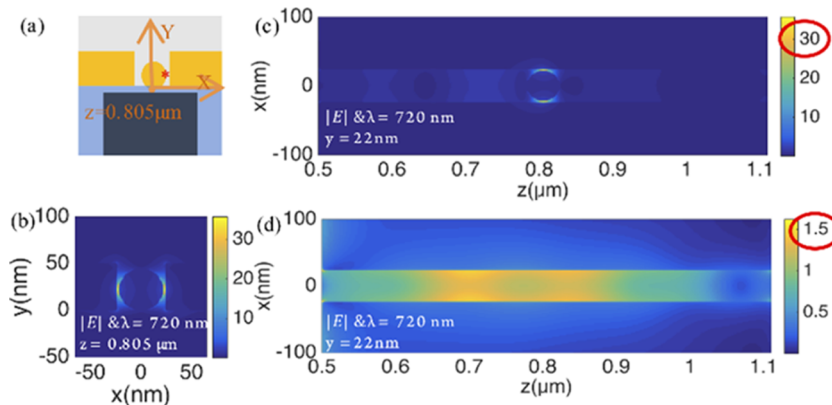

Figure 3. SPP−LSP coupling in the gold sphere−slot junction: (a) z-normal cross section of a 44 nm diameter sphere at the center of the slot bottom. (b, c) $|E|$ local electric field distributions on the plane: (b) $z = 0.805$ μm and (c) $y = 22$ nm at $\lambda = 720$ nm. (d) $|E|$ field distribution on the plane $y = 22$ nm at $\lambda = 720$ nm before the in-slot sphere is added.

plasmonic modes couple back into the Si$_3$N$_4$ strip and finally to the spectrometer. The $|E|$ field distribution on an x-normal plane with $x = 24$ nm (across a slot wall) is presented in Figure 1c when the fundamental TE mode of the Si$_3$N$_4$ strip is injected at $z = 0.25$ μm as the incidence. It is worth noting that all of the electric field in this study is normalized with the maximum value of the incident electric field. Figure 2 shows the charge distributions on the slot walls. It is seen that the SPP is excited in the slot and particularly the electric field around the slot corners is obviously stronger than that in the strip. The in-slot field distributed along the z-axis has some fluctuations, which come from the in-slot SPP interferences caused by the reflection of the slot's facets. To some degree, the finitely long metallic slot can be taken as a cavity and it traps the SPP modes insides. The strip−slot coupling is the route to exchange energy between the cavity (slot) and the exterior (strip).

If a metallic nanoparticle is added into the slot, then there will be a strong SPP−LSP interaction and intense electric field between the nanoparticle and the slot walls. We focus on this interaction and the enhancement in the particle−slot junction in this study. The sensor structure in Figure 1 is always kept as the same in the following discussion with metallic nano-particles.

RESULTS AND DISCUSSION

To confine the electric field into a small area or gap in the sensor's slot, one method is making the in-slot metallic particle size close to the slot width. Then, the gaps between the particle and the slot walls can be limited in a few nanometers, which can act as the hotspots for SERS. Here, assuming that a gold sphere with a 44 nm diameter is placed at the bottom center of the 48 nm wide slot with center coordinates $x = 0$ nm, $y = 22$ nm, and

$z = 0.805$ μm, as shown in Figure 3a, two 2 nm wide gaps are created in the sphere−slot junction. With the fundamental TE mode of the Si$_3$N$_4$ strip as the incident light, the in-slot SPP is excited and it excites the electron oscillation of the gold sphere in its propagation. As shown in Figure 3b,c, the intense local electric field appears in the 2 nm wide gaps of the sphere−slot junction. Compared to the $|E|$ field distribution in Figure 3d, which is the case without the gold sphere, the field intensity with the sphere, particularly in the sphere−slot wall gaps, is raised dramatically. If analyte molecules are in these gaps, their Raman scatterings can be strongly enhanced. Therefore, these hotspots around the in-slot particle can be regarded as the probe volume of the sensor. In this study, we define the probe volume by a cuboid: $[-W/2 < x < W/2; 0 < y < H; Zc_{sphere} - R_{sphere} < z < Zc_{sphere} + R_{sphere}]$, where Zc_{sphere} is the z coordinate of the sphere center and R_{sphere} is the sphere radius. If not specified otherwise, the probe volume is kept the same in the following discussion.

SPP−LSP Coupling. To demonstrate clearly the SPP−LSP coupling in the gold sphere−slot junction, the attention is first placed in the case of a sphere and an infinite slot, which avoids the interferences of the in-slot SPP in the sensor described in Figure 1. As shown in the top inset of Figure 4, the slot is infinite in the $+z$ direction and a gold sphere with diameter 44 nm is assumed to be located in the slot. The absorption curves of the gold sphere in the infinite slot are reported in Figure 4. The absorption of the same gold sphere without the gold slot (as shown in the bottom inset) is also included for comparison. It is seen that the peak 546 nm does not appear in the absorption curves of the in-slot spheres. That means this peak (resulting from the direct interaction of the sphere and the Si$_3$N$_4$ strip) is suppressed in the hybridization of the in-slot SPP
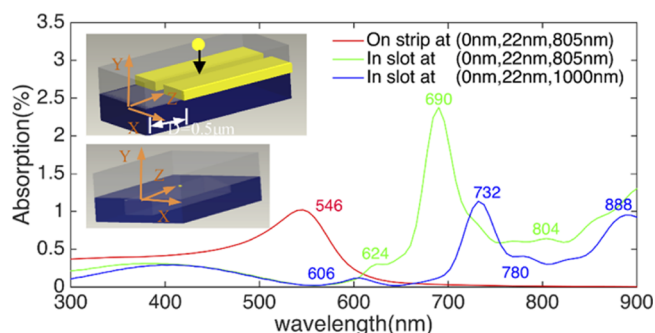
Figure 4. Absorptions of a 44 nm diameter gold sphere in the infinite slot with center coordinates: $x = 0$ nm, $y = 22$ nm, and $z = 805/1000$ nm (top inset) and the same sphere with coordinates: $x = 0$ nm, $y = 22$ nm, and $z = 805$ nm when the slot is removed (bottom inset).

and the in-sphere LSP. When the z-axis position of the in-slot sphere changes from $z = 0.805$ to 1.0 μm, the highest absorption peak decreases and shifts from 690 to 732 nm. This is reasonable because the in-slot SPP fields distribute in the beating pattern along the z-axis direction and the strongest electromagnetic fields of different wavelengths appear at different z-axis positions.

When the slot of the sensor is finite, as shown in the inset of Figure 5, the absorption curve of the in-slot sphere is reported
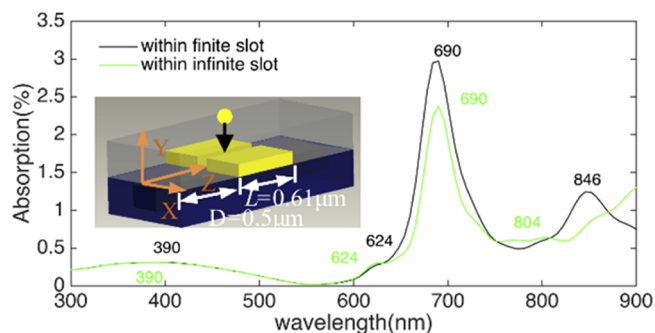

Figure 5. Absorptions of the 44 nm diameter gold sphere located at $x = 0$ nm, $y = 22$ nm, and $z = 805$ nm when it is in an infinite/finite slot. The inset shows the case of the finite slot and the geometry is the same as that in Figure 1a,b.

below. For comparison, the green absorption curve of the sphere in the infinite slot in Figure 4 is also included. Compared to the case of the infinite slot, the sphere in the sensor's finite slot has a new peak at 846 nm. The SPP fields of the finite slot are modulated constructively or destructively by the interferences, as shown in Figure 3c,d, which are the excitation source of the in-sphere LSP. Subsequently, the in-sphere plasmons are shaped by the interferences, leading to the appearance of the new peak at 846 nm. Besides that, the absorption peak at 960 nm is constant no matter whether the slot is infinite or finite. The charge distributions of the sphere–slot (infinite and finite) junctions for the peaks at 690 nm are shown in Figure 6. It is obvious that the electron oscillations in the sphere–slot junction are much stronger than those on the slot walls. If the local slot walls in the junction are taken as a metallic pseudonanoparticle, the charge distributions are the typical light mode in the hybridization of two particles. For convenience, the oscillation modes of the electrons in the sphere–slot junction are noted as localized SPP–LSP modes,

which result from the hybridization of the SPP in the finite slot and the LSP in the sphere.

To discuss the SERS enhancement in the sphere–slot wall gaps, one example point is chosen at coordinates (23, 22 nm, 0.805 μm). This point is the center of the right sphere–slot wall gap marked by a red star in Figure 3a. It has been mentioned before that all of the electric field in this study is normalized with the maximum value of the incident electric field. So, the $|E|^4$ approximation can be simplified as EF $= |E_{Loc}/E_{ref}|^4 = |E_{Loc}|^4$ when the reference electric field E_{ref} is chosen as the maximum value of the incident electric field. According to the local electric field E_{Loc}, the enhancement factor of the example point is reported in Figure 7. The $|E|^4$ approximation, which is used extensively to estimate EFs in the literature of SERS, has been proven to be valid in this calculation by our previous works.[14] The EF curves of the same point in the cases with the isolated sphere and the isolated slot are also included for comparison. We note that only the wavelength range from 600 to 900 nm is concerned for the EF discussion because the coupling between the strip and the slot is very weak when the wavelength is smaller than 600 nm. When the sphere–slot junction is present, the EF of the example point is raised to a level of 10^6 at 693 nm, 4 orders of magnitude higher than the isolated slot or sphere. A shoulder (639 nm) and two peaks (693, 847 nm) appear in the red solid EF curve. The charge distributions of the sphere–slot junction corresponding to the three wavelengths are presented in Figure 8. If grouping these modes by the sphere charge, we can see that the shoulder at 639 nm comes from one quadrupole mode and the two other peaks come from two dipole modes. The three wavelengths agree with the shoulder and the peaks of the black absorption curve in Figure 5. When only the finite slot exists above the embedded strip, two peaks at 654 and 781 nm appear in the EF curve of the sample point in Figure 7. This is because the local electric field of the example point is constructively or destructively interfered along the z-axis direction due to the facet reflection in the finite slot.

Multifactor Dependence of the EFs in the Probe Volume. We have discussed the SPP–LSP coupling between the slot and the sphere on the basis of the assumption that a gold sphere is located at the bottom center of the slot of the sensor. However, it would be very difficult to accurately put a particle at a desired position in a nanoscale slot in actual experiments. The sphere's position is directly related to the sphere–slot wall gap size (transverse position) and the intensity of the local SPP (longitudinal position). So, the enhancement for Raman scatterings around the sphere is inevitably affected by the sphere's position.

To show the influence of the sphere's transverse (x axis) position on the enhancement in the probe volume, a transverse offset of $+1$ or $+2$ nm is added to the sphere in Figure 3a. With the offsets, the sphere–slot wall gaps are modified with width = 1, 3 and 4, 0 nm (wedge gap), respectively. The averaging enhancement factors of the probe volume around the sphere are reported in Figure 9. The case with no transverse offset of the sphere is also included for comparison. We know that a transverse offset of the sphere position would narrow one of the sphere–slot wall gaps and a narrower gap can confine the electric field further with the more intense intensity. So, the offset increases the enhancement around the sphere. Comparing the red and green curves in Figure 9, it is seen that the EF peaks show a red shift with a transverse offset. When the offset is $+2$ nm, the sphere touches the slot wall and the sphere–slot
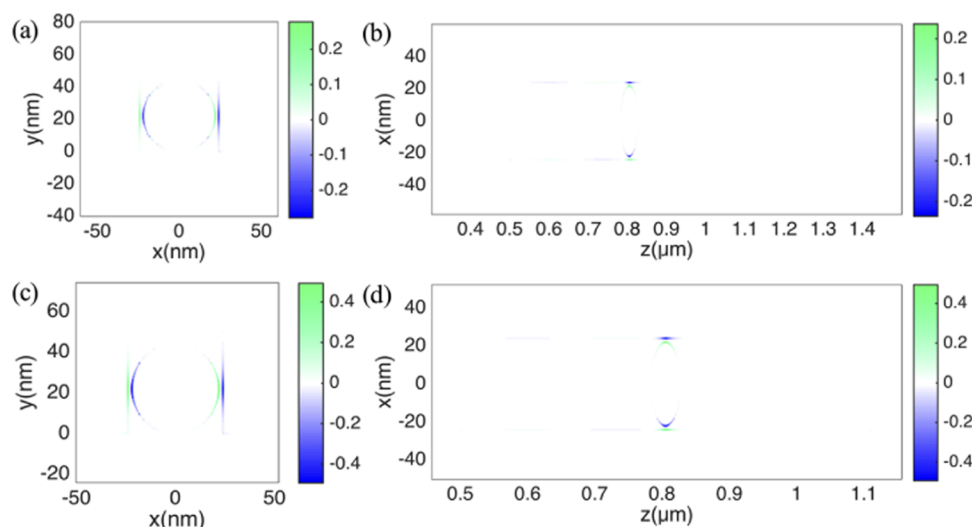
Figure 6. Charge distributions of the sphere−slot (infinite and finite) junctions for the peaks at 690 nm in Figure 5. (a) and (b) for the infinite slot and (c) and (d) for the finite slot. (a, c) z-Normal plane with $z = 0.805\ \mu m$; (b, d) y-normal plane with $y = 22$ nm.
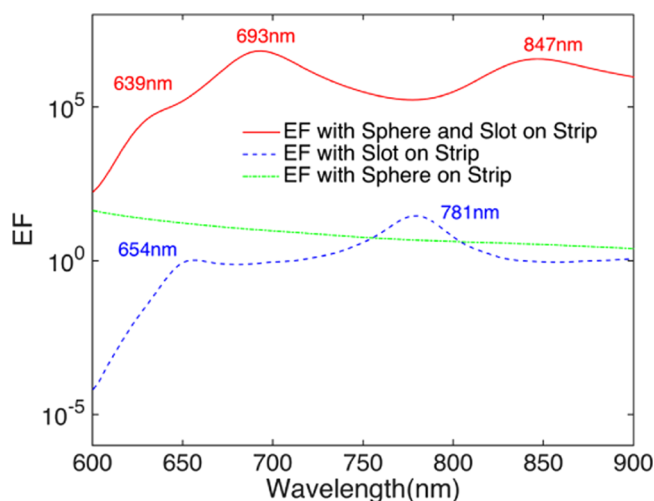

Figure 7. Enhancement factors based on the $|E|^4$ approximation of the example point, which is marked by a red star at 23, 22 nm, and 0.805 μm in Figure 3a, involving three cases: the gold sphere, the gold slot, and the gold sphere−slot junction.

wall gap becomes a wedge gap. It has the sharpest nanostructure, leading to the highest enhancement factor around the sphere. On the other hand, there is no SPP−LSP hybridization when the particle touches the slot wall. Therefore, its curve shapes of the averaging and maximum EFs are different from the other two cases in Figure 9. The inset graph presents the maximum enhancement factors of the probe volume around the sphere. The max EFs are 10^4 times higher than the corresponding averaging values. The EF curves of the maximum and averaging values in the probe volume have the similar curve shapes.

When the sphere has the longitudinal (z-axis) position $z = 0.6$, 0.7, and 0.805 μm with $x = 0$ nm and $y = 22$ nm, the enhancement factors of the probe volume are reported in Figure 10. We note that the optical reciprocity of Raman excitation and radiation is broken because the sphere deviates from the longitudinal middle of the metallic slot (details can be found in the Supporting Information). Then, the $|E|^4$ approximation is modified as EF = $|E_{x,y,z}|^2 \times |E_{x,y,1.61\ \mu m-z}|^2$.

Because of the symmetry, the EFs in the two half ranges of the slot from $z = 0.5$ to 0.805 μm and $z = 0.805$ to 1.11 μm are symmetrical. We only analyze the first range here. The longitudinal position does not change the sphere−slot wall gap size, so the enhancement factors in the probe volume stay at similar levels in Figure 10, 10^4 for the averaging value and 10^6 for the maximum value. On the other hand, the EF curve shape has an obvious change when the sphere's longitudinal position changes. The reason is that the in-slot local SPP fields change along the longitudinal direction. It has been mentioned before that the in-slot SPP fields distribute in the beating pattern along the z-axis direction and that the strongest/weakest electromagnetic fields of different wavelengths appear at different z-axis positions. Moreover, along the longitudinal direction, the SPP electric field is affected by the constructive or destructive interferences caused by the slot facet reflection. The sphere is excited directly by the in-slot SPP and subsequently the in-sphere plasmons are also shaped by the longitudinal change of the SPP intensity. So, the sphere's longitudinal position would change the SPP−LSP modes in the sphere−slot junction. The electric field distributions of all of the peaks in Figure 10 are shown in Figure S2 of the Supporting Information.

When the sphere diameter changes, the enhancement around the sphere would be modified due to the size change of the sphere−slot wall gaps. This is a little similar to the change of the sphere's transverse position that has been discussed. The averaging and maximum enhancement factors of the probe volume around the sphere with different diameters are presented in Figure 11. The bigger diameter results in a red shift of the three localized SPP−LSP modes of the sphere−slot junction. Because of the size decrease of the sphere−slot wall gaps and more intense local electric field, the enhancement factors in the sphere−slot junction increases when the sphere becomes bigger. However, putting a bigger sphere into the slot would become more difficult. It also impedes the analyte molecules from entering into the gaps if the sphere−slot wall gaps are too small.

Except for the sphere, the in-slot particle can have other shapes, such as cube and cylinder. The enhancement factors of the probe volume around the particles with different shapes are presented in Figure 12. The sphere case is also included for
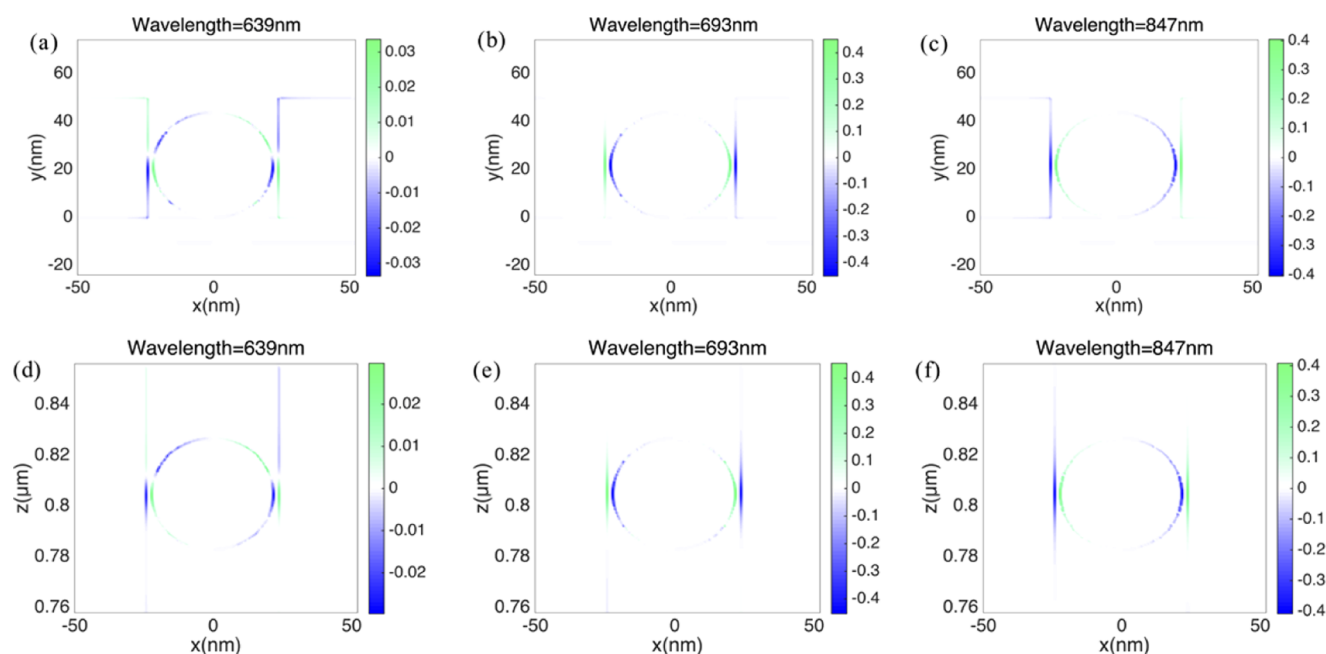
Figure 8. Charge distributions on the z-normal cross section through the sphere−slot junction with $z = 0.805 \, \mu m$ in (a)−(c) and on the y-normal cross section through the sphere−slot junction with $y = 22$ nm in (d)−(f) corresponding to the localized SPP−LSP modes of the red EF curve in Figure 7.
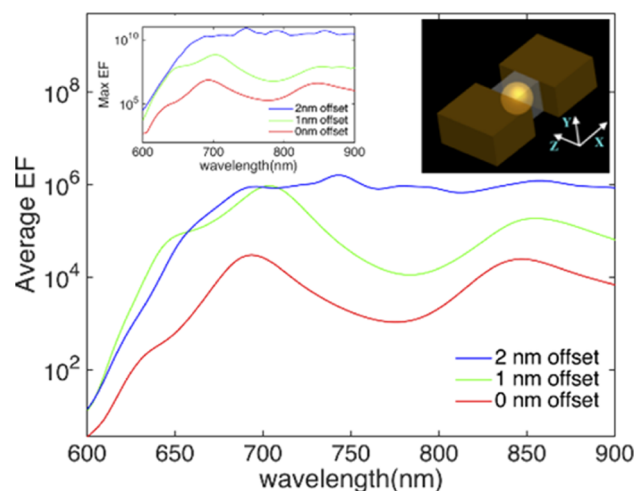

Figure 9. Averaging enhancement factors of the cuboid probe volume when the sphere position has a transverse offset 0, 1, or 2 nm, respectively, with center coordinates $x = 0$, 1, or 2 nm; $y = 22$ nm; and $z = 0.805 \, \mu m$. The inset graph shows the maximum enhancement factors in the probe volume. In the inset image, the white cuboid shows the probe volume around the sphere.

Figure 10. Averaging enhancement factors of the cuboid probe volume when the sphere has the longitudinal position $z = 0.6$, 0.7, and 0.805 μm with the other center coordinates $x = 0$ nm and $y = 22$ nm. The inset graph shows the maximum enhancement factors in the probe volume. In the inset image, the white cuboid shows the probe volume around the sphere.

comparison. The sizes of all of the particles are the same, i.e., 44 nm, and they are located at the bottom center of the slot, like the sphere in Figure 3a. All of the gaps of the particle−slot junctions are 2 nm wide, so the averaging enhancement factors around these particles are on the similar order of magnitude. Compared to the others, the cube has one more peak on the red EF curve. This is because the cube has more LSP modes in free space and so as the SPP−LSP modes in the cube−slot junction. The electric field distributions of the peaks and shoulders in Figure 12 are presented in Figure S3 of the Supporting Information.

We have discussed the cases in which the particle size (42−46 nm) is just a little smaller than the slot width, 48 nm. There
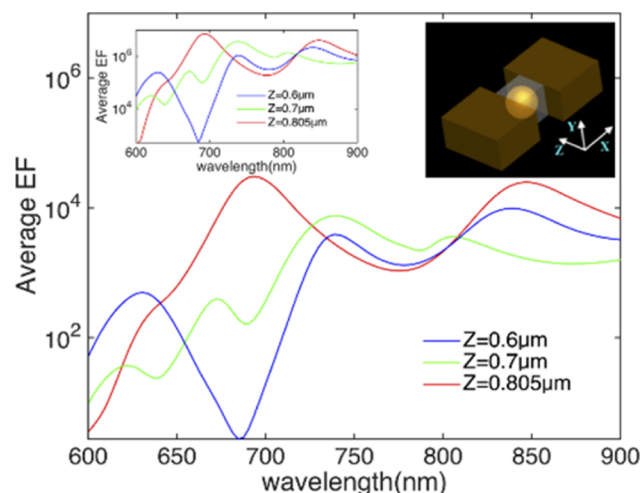
may be a problem in actual experiments when putting the particle into the nanoscale slot. An intuitive way to solve this problem is decreasing the particle size. If some surface functional technologies are used, the particles can be immobilized near the slot walls to create some small particle−slot wall gaps. Then, the strong enhancement for Raman scatterings can still be obtained in the particle−slot junction. The enhancement factors of the probe volume around some very small particles that are close to the slot walls are shown in Figure 13. All of the particle−slot wall gaps are 2 nm wide. Here, we note that the probe volume is redefined. It is seen that all of the EF curves have two peaks around 650 and 770 nm. At these peaks, the in-sphere electrons oscillate in a
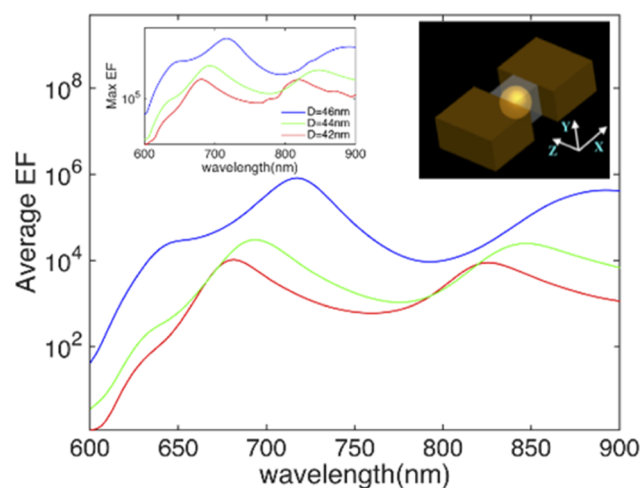
Figure 11. Averaging enhancement factors of the cuboid probe volume when the sphere diameter is D = 42, 44, and 46 nm with center coordinates x = 0 nm; y = 21, 22, and 26 nm; and z = 0.805 μm. The inset graph is the maximum enhancement factors in the probe volume. In the inset image, the white cuboid shows the probe volume around the sphere.
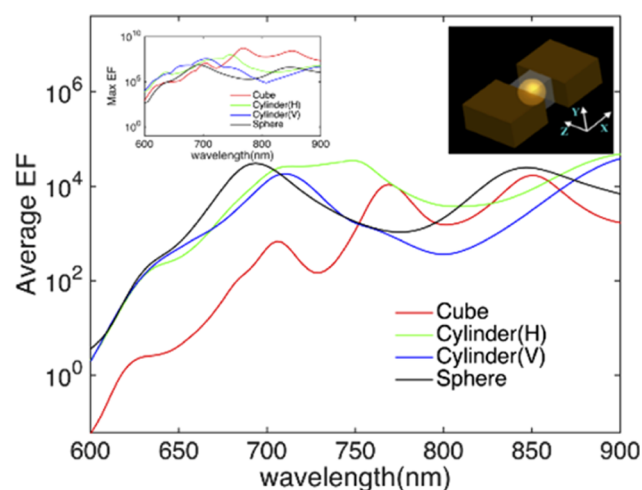

Figure 13. Averaging enhancement factors of the cuboid probe volume when the in-slot particle has different shapes with the same center coordinates x = 17 nm, y = 5 nm, and z = 0.805 μm. The cube side is 10 nm. The height and diameter of the cylinder are both 10 nm. When the axis of the cylinder is along the z/y-direction, it is marked with "H"/"V". The sphere diameter is 10 nm. The inset graph shows the maximum enhancement factors in the same volume. In the inset image, the white cuboid shows the probe volume around the particle (the cylinder "V", for instance). Here, the probe volume is redefined as: [10 nm < x < 24 nm; 0 < y < 12 nm; 800 nm < z < 810 nm].

Figure 12. Averaging enhancement factors of the cuboid probe volume when the particle has different shapes with the same center coordinates x = 0 nm, y = 22 nm, and z = 0.805 μm. The cube side is 44 nm. The height and diameter of the cylinder are both 44 nm. When the axis of the cylinder is along the z/y-direction, it is marked with "H"/"V". The sphere diameter is 44 nm. The inset graph shows the maximum enhancement factors in the same volume. In the inset image, the white cuboid shows the probe volume around the particles (the sphere, for instance).

dipole mode, which is known from the electric field distributions around the particles presented in Figure S4 of the Supporting Information. The two wavelengths 650 and 770 nm are similar to the peak positions 654 and 781 nm of the blue dash curve in Figure 7, which for the EF of the sample point without the in-slot particle. That means that the influence of the in-slot particles with diameter 10 nm on the in-slot field distribution is almost negligible after the particles are added into the slot. The localized SPP−LSP modes in the particle−slot junction are mainly determined by the interfered SPP of the slot, whereas the in-sphere LSP does not obviously influence the resonant wavelengths of the junction. So, the EF curves of the probe volume around the small particles have
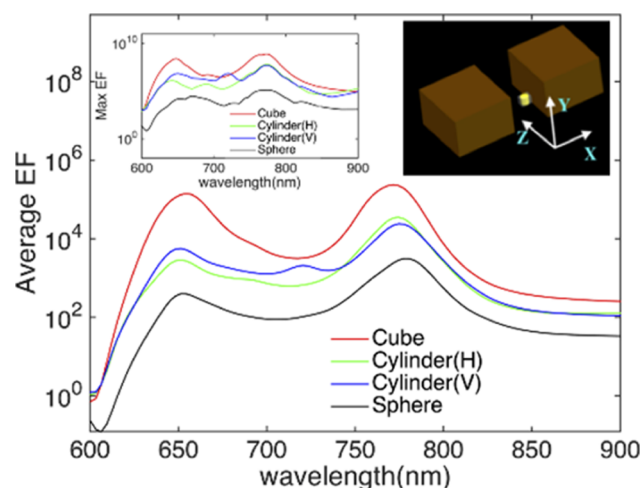
peak positions similar to the EF peaks of the sample point before the particles are added. In Figure 13, the cube has the largest enhancement factor, whereas the sphere has the smallest one.

To obtain more hotspots or probe volumes in the sensor, an intuitive method is to put more nanoparticles into the slot. The averaging enhancement factors of the probe volume when two gold spheres are added into the sensor's slot are reported in Figure 14. When the sphere diameter is 44 nm, the two particles are located with center coordinates x = 0 nm, y = 22 nm, and z = 0.805/1.0 μm. When the diameter of the two spheres is 10 nm, they are placed at z = 17 nm, y = 22 nm, and z = 0.805/1.0 μm. The 44 nm diameter spheres have two 2 nm gaps with the slot walls, whereas the 10 nm diameter spheres have one 2 nm sphere−slot wall gap. Here, the probe volume around the 10 nm diameter spheres is redefined as that in Figure 13. When the two in-slot spheres have the diameter D = 44 nm, it is seen that the highest peak (1.60×10^4 at λ = 696.5 nm) of the red EF curve for the probe volume around the first sphere is lower than the maximum EF value (3.05×10^4 at λ = 693.5 nm) of the red EF curve in Figure 9. It means that the enhancement effect in the probe volume of the first gold sphere decreases due to adding the second sphere into the slot. The green EF curve of the second sphere with diameter 44 nm is much lower than the first sphere because the first sphere impedes the in-slot SPP to reach the second sphere. It is seen in Figure 15a that the field |E| in the slot with z > 0.805 μm is obviously weaker than the range z < 0.805 μm. When the diameter of the two in-slot spheres is 10 nm, the impediment of the first sphere for the SPP propagation is smaller, as shown in Figure 15b. It is seen that the highest peak (3.42×10^3 at λ = 780.5 nm) of the blue EF curve around the first sphere is similar with the maximum EF value (3.33×10^3 at λ = 777.5 nm) of the black EF curve in Figure 13. It means that there is almost no EF reduction for the first sphere after the second one
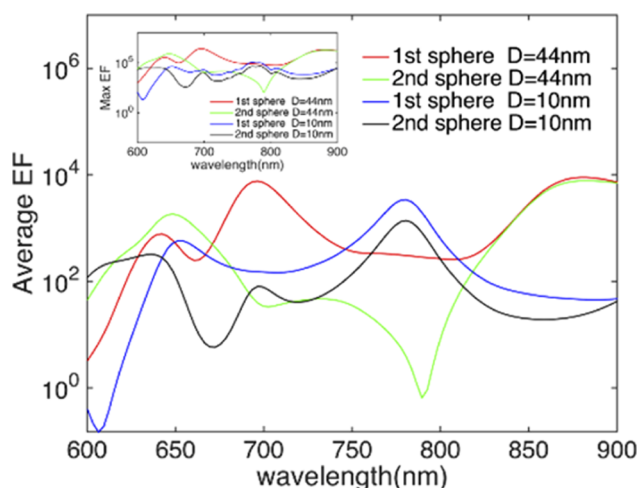
Figure 14. Averaging enhancement factors of the cuboid probe volume when two gold spheres are added into the sensor's slot. When the two in-slot spheres have the diameter 44 nm, the first sphere is located with center coordinates $x = 0$ nm, $y = 22$ nm, and $z = 0.805$ μm (like that in Figure 3a) and the second one is placed with $x = 0$ nm, $y = 22$ nm, and $z = 1.0$ μm. When the two in-slot spheres have the diameter 10 nm. The first gold sphere is located with center coordinates $x = 17$ nm, $y = 5$ nm, and $z = 0.805$ μm (like that in Figure 13) and the second one is placed with $x = 17$ nm, $y = 5$ nm, and $z = 1.0$ μm. The edge-to-edge distances between the spheres are 185 nm (the diameter is 10 nm) and 151 nm (the diameter is 44 nm). The inset graph shows the maximum enhancement factors in the probe volume. Here, the probe volume of the 10 nm diameter sphere is redefined as: [10 nm < x < 24 nm; 0 < y < 12 nm; 800 nm < z < 810 nm].
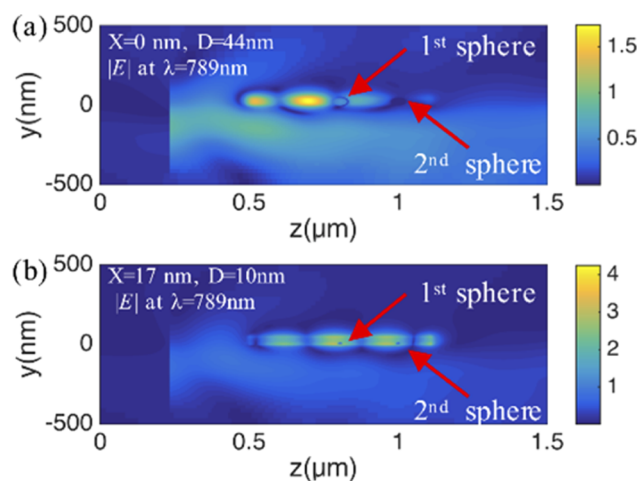

Figure 15. |E| field distributions at $\lambda = 789$ nm (a) on an x-normal plane across the center of the in-slot particles with the diameter $D = 44$ nm and (b) on an x-normal plane across the center of the in-slot particles with the diameter $D = 10$ nm.

is added into the slot if its diameter is 10 nm. So, if the particle size is big, it is not suggested to put many metallic particles into the sensor's slot. If the particles are small, more than two particles could be employed in the slot to obtain more hotspots and output more Raman signals.

When the diameter of two in-slot metallic particles is 10 nm, there is a possibility that the two particles arrange along the x-axis direction. The enhancement factors around two gold spheres arranging in the x-axis direction are presented in Figure

16. The black EF curve in Figure 13 is also included for comparison. The sphere−sphere gap is assumed to be 2 nm. In
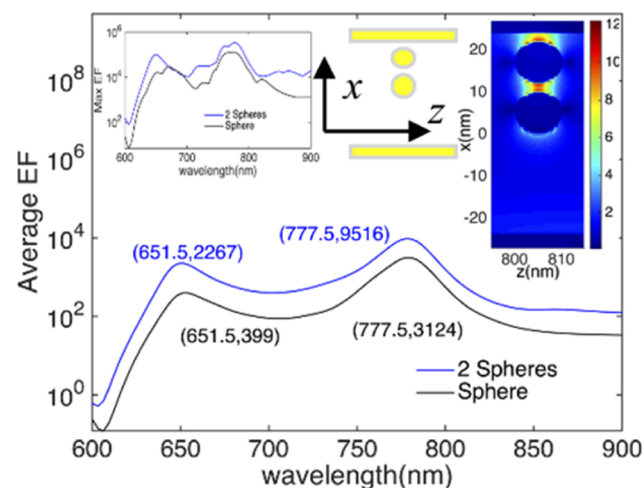

Figure 16. Averaging enhancement factors of the cuboid probe volume when two gold spheres are added into the sensor's slot and arranged along the x-axis direction. The two in-slot spheres have the diameter 10 nm. The first gold sphere is located with center coordinates $x = 17$ nm, $y = 5$ nm, and $z = 0.805$ μm (like that in Figure 13) and the second one is placed with $x = 5$ nm, $y = 5$ nm, and $z = 1.0$ μm. The black EF curve in Figure 13 is also included for comparison. The sphere−sphere gap is 2 nm. The inset graph shows the maximum enhancement factors in the probe volume. Here, the probe volume of the 10 nm diameter sphere is defined as: [10 nm < x < 24 nm; 0 < y < 12 nm; 800 nm < z < 810 nm].

the inset |E| image, it is seen that the second sphere is excited by the LSP on the first sphere and intense electric field appears in the sphere−sphere gap. Compared to the case of one particle, the enhancement factors of the same cuboid probe volume can be bigger. For example, the averaging enhancement factor increases 3 times from 3124 to 9516 at 777.5 nm. When the two particles have another shape (cube and cylinder), the enhancement factors of the same probe volume are shown in Figure S5 of the Supporting Information.

Characterization of the SERS Detection Capability. To characterize the SERS detection capability of the sensor quantitatively, the sensor with a 44 nm diameter gold sphere at the bottom center of the slot, which is described in Figure 3a, is chosen as an example here. The EF average of the probe volume is 3.052×10^4 when the excitation wavelength is 693.5 nm, as shown by the red EF curve in Figure 9. The excitation power is assumed to be 10 mW, and the excitation wavelength is 693.5 nm. The lowest detectable power of the detector refers to the Ocean Optics QE65 Pro spectrometer. The Raman-active dyes, rhodamine 6G (RH6G) and benzotriazole dye 2 (BTZ), are chosen as the probe molecules, which are dissolved in distilled water. For simplicity, the depolarization ratio of the Raman tensor ρ_R is assumed to be 0 and the molecules distribute in the probe volume uniformly. Under the two assumptions, the Raman signal intensity (electron number per second) given out by the SERS sensor is reported in Figure 17. The typical Raman spectra of RH6G and BTZ are shown in the inset, which is reproduced from ref 6. It is seen that the RH6G solution with concentration of 1.36×10^{-5} mol/L and the BTZ solution with concentration of 1.13×10^{-4} mol/L are detectable by the sensor at room temperature. If the detector is cooled, BTZ can be detected with concentration of $6.06 \times$
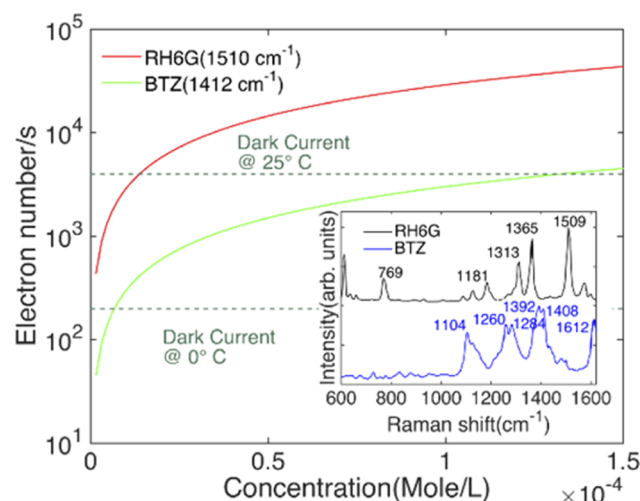
Figure 17. Electron number per second excited by the Raman signals of RH6G and BTZ on the detector of an Ocean Optics QE65 Pro spectrometer. The SERS sensor has a gold sphere with diameter 44 nm at the bottom center of the slot, as shown in Figure 3a. The two black lines are the dark current of the spectrometer. The inset shows the typical Raman spectra of RH6G and BTZ.[6]

10^{-6} mol/L. If the in-slot gold sphere has a 2 nm transverse offset, the EF average of the probe volume will increase to 9.10×10^5 at $\lambda = 693.5$ nm, as shown by the blue EF curve in Figure 6. Then, the lowest detectable concentration in Figure 17 can be decreased 30 times.

CONCLUSIONS

In this study, we have investigated theoretically the effect of in-slot metallic nanoparticles on improving the detection capacity of the SERS sensor. We have first investigated the SPP–LSP coupling between the metallic slot and the metallic nanoparticle. It is found that the localized SPP–LSP modes appear in the metallic sphere–slot junction because of the electromagnetic hybridization of the in-slot metallic particle and the finite slot (a half-open cavity). The influences of the particle position, size, shape, and number on the enhancement in the probe volume around the in-slot particle have been investigated adequately to point out the strategy to optimize the sensing performance. The gold particles in the sensor's slot can make several molecule detections possible in the sensor by providing averaging EFs as high as 10^6 in the probe volume. To characterize quantitatively the sensor's SERS detection capacity, a specific sensor with a 44 nm diameter gold sphere at the bottom center of the slot is chosen as an example here. It is seen that the RH6G solution with 1.36×10^{-5} mol/L and the BTZ solution with 1.13×10^{-4} mol/L are detectable at room temperature by the sensor. In realistic detections, the metallic nanoparticles can be synthesized chemically, such as the citrate-reduced gold colloids, which are centrifuged to get the particles. Then, the diluted particle solution can be dripped and dried on the sensor's slot directly or functionalized by surface techniques such as ligand-exchange with aqueous thiol molecules. These results demonstrate that a SERS detection system with high enhancement factors can be realized on a compatible chip based on our SERS sensor with metallic nanoparticles.

METHODS

All of the simulations in this study are implemented by the three-dimensional finite-difference time domain (3D-FDTD) algorithm with the commercial software package FDTD solutions provided by Lumerical Solutions, Inc. The simulation region was set as a cuboid volume of 1 μm × 1 μm × 1.5 μm, with perfectly matched layers as the six boundaries. All of the objects, sources, and monitors were laid in this simulation volume. The dielectric function data of silicon nitride (Si_3N_4) were referred to the experimental data obtained in ref 21. All of the other optical constants were taken directly from the database of the FDTD software.

ASSOCIATED CONTENT

Ⓢ Supporting Information

The Supporting Information is available free of charge on the ACS Publications website at DOI: 10.1021/acsomega.7b02020.

Schematic representation of the optical reciprocity in the Raman sensor; electric field |**E**| distributions; averaging enhancement factors of the cuboid probe volume (PDF)

AUTHOR INFORMATION

Corresponding Authors
*E-mail: salim.boutami@cea.fr (S.B.).
*E-mail: pierre_michel.adam@utt.fr (P.-M.A.).
ORCID Ⓘ
Salim Boutami: 0000-0001-6611-5159
Notes
The authors declare no competing financial interest.

REFERENCES

(1) Sharma, B.; Frontiera, R. R.; Henry, A.-I.; Ringe, E.; Van Duyne, R. P. SERS: Materials, Applications, and the Future. *Mater. Today* **2012**, *15*, 16–25.

(2) McNay, G.; Eustace, D.; Smith, W. E.; Faulds, K.; Graham, D. Surface-Enhanced Raman Scattering (SERS) and Surface-Enhanced Resonance Raman Scattering (SERRS): A Review of Applications. *Appl. Spectrosc.* **2011**, *65*, 825–837.

(3) Bantz, K. C.; Meyer, A. F.; Wittenberg, N. J.; Im, H.; Kurtuluş, Ö.; Lee, S. H.; Lindquist, N. C.; Oh, S.-H.; Haynes, C. L. Recent Progress in SERS Biosensing. *Phys. Chem. Chem. Phys.* **2011**, *13*, 11551–11567.

(4) Cialla, D.; März, A.; Böhme, R.; Theil, F.; Weber, K.; Schmitt, M.; Popp, J. Surface-Enhanced Raman Spectroscopy (SERS): Progress and Trends. *Anal. Bioanal. Chem.* **2012**, *403*, 27–54.

(5) Murphy, T.; Lucht, S.; Schmidt, H.; Kronfeldt, H. Surface-enhanced Raman Scattering (SERS) System for Continuous Measurements of Chemicals in Sea-water. *J. Raman Spectrosc.* **2000**, *31*, 943–948.

(6) Le Ru, E.; Etchegoin, P. *Principles of Surface-Enhanced Raman Spectroscopy: And Related Plasmonic Effects*; Elsevier, 2008.

(7) Hiep, H. M.; Endo, T.; Kerman, K.; Chikae, M.; Kim, D.-K.; Yamamura, S.; Takamura, Y.; Tamiya, E. A Localized Surface Plasmon Resonance Based Immunosensor for the Detection of Casein in Milk. *Sci. Technol. Adv. Mater.* **2007**, *8*, 331–338.

(8) Svedendahl, M.; Chen, S.; Dmitriev, A.; Kall, M. Refractometric Sensing Using Propagating versus Localized Surface Plasmons: A Direct Comparison. *Nano Lett.* **2009**, *9*, 4428−4433.

(9) Camden, J. P.; Dieringer, J. A.; Wang, Y.; Masiello, D. J.; Marks, L. D.; Schatz, G. C.; Van Duyne, R. P. Probing the Structure of Single-Molecule Surface-Enhanced Raman Scattering Hot Spots. *J. Am. Chem. Soc.* **2008**, *130*, 12616−12617.

(10) Holmstrom, S. A.; Stievater, T. H.; Kozak, D. A.; Pruessner, M. W.; Tyndall, N.; Rabinovich, W. S.; McGill, R. A.; Khurgin, J. B. Trace Gas Raman Spectroscopy Using Functionalized Waveguides. *Optica* **2016**, *3*, 891−896.

(11) Ismail, N.; Choo-Smith, L.-P.; Wörhoff, K.; Driessen, A.; Baclig, A.; Caspers, P.; Puppels, G.; De Ridder, R.; Pollnau, M. Raman Spectroscopy with an Integrated Arrayed-Waveguide Grating. *Opt. Lett.* **2011**, *36*, 4629−4631.

(12) Ackermann, K. R.; Henkel, T.; Popp, J. Quantitative Online Detection of Low-Concentrated Drugs via a SERS Microfluidic System. *ChemPhysChem* **2007**, *8*, 2665−2670.

(13) Ismail, N.; Baclig, A. C.; Caspers, P. J.; Sun, F.; Wörhoff, K.; de Ridder, R. M.; Pollnau, M.; Driessen, A. *Design of Low-Loss Arrayed Waveguide Gratings for Applications in Integrated Raman Spectroscopy*; Optical Society of America, 2010; p CFA7.

(14) Tang, F.; Adam, P.-M.; Boutami, S. Theoretical Investigation of SERS Nanosensors Based on Hybrid Waveguides Made of Metallic Slots and Dielectric Strips. *Opt. Express* **2016**, *24*, 21244−21255.

(15) Delacour, C.; Blaize, S.; Grosse, P.; Fedeli, J. M.; Bruyant, A.; Salas-Montiel, R.; Lerondel, G.; Chelnokov, A. Efficient Directional Coupling between Silicon and Copper Plasmonic Nanoslot Waveguides: Toward Metal-Oxide-Silicon Nanophotonics. *Nano Lett.* **2010**, *10*, 2922−2926.

(16) Mock, J. J.; Hill, R. T.; Degiron, A.; Zauscher, S.; Chilkoti, A.; Smith, D. R. Distance-Dependent Plasmon Resonant Coupling between a Gold Nanoparticle and Gold Film. *Nano Lett.* **2008**, *8*, 2245−2252.

(17) Chu, Y.; Crozier, K. B. Experimental Study of the Interaction between Localized and Propagating Surface Plasmons. *Opt. Lett.* **2009**, *34*, 244−246.

(18) Ghoshal, A.; Divliansky, I.; Kik, P. G. Experimental Observation of Mode-Selective Anticrossing in Surface-Plasmon-Coupled Metal Nanoparticle Arrays. *Appl. Phys. Lett.* **2009**, *94*, No. 171108.

(19) DiMaria, J.; Paiella, R. Plasmonic Dispersion Engineering of Coupled Metal Nanoparticle-Film Systems. *J. Appl. Phys.* **2012**, *111*, No. 103102.

(20) Fang, Y.; Wei, H.; Hao, F.; Nordlander, P.; Xu, H. Remote-Excitation Surface-Enhanced Raman Scattering Using Propagating Ag Nanowire Plasmons. *Nano Lett.* **2009**, *9*, 2049−2053.

(21) Philipp, H. R. Optical Properties of Silicon Nitride. *J. Electrochem. Soc.* **1973**, *120*, 295−300.